Supplementary Materials for

Evolution and structural plasticity of microvilli

Silin Zhang[1]†, Fang Kong[1]†, Jiaxin Tan[1]†, Yang Shen[1], Tianwei Zhao[1], Shanjin Huang[1], Chuangye Yan[1]*

Corresponding author: yancy2019@tsinghua.edu.cn

The PDF file includes:

Figures S1 to S12

Table S1 to S2

Movies S1 to S4

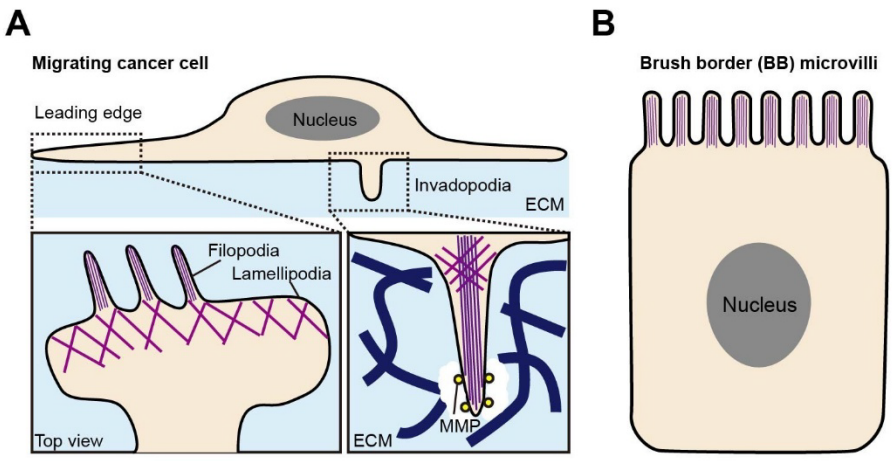


Figure S1. Representative architectures and functions of major actin-based protrusions

(A) Schematic illustration of actin-based protrusions associated with cell migration and invasion. At the leading edge of a migrating cancer cell, lamellipodia form broad sheet-like protrusions, whereas filopodia extend as finger-like actin bundles that probe the extracellular environment. Invadopodia penetrate the extracellular matrix (ECM) and concentrate matrix metalloproteinases (MMPs) to facilitate matrix degradation and invasion. Insets show the characteristic actin architectures of these protrusions. **(B)** Schematic representation of brush border microvilli. Microvilli are stable actin-supported membrane protrusions that densely decorate the apical surface of epithelial cells, forming highly ordered parallel arrays specialized for absorption and environmental sensing.

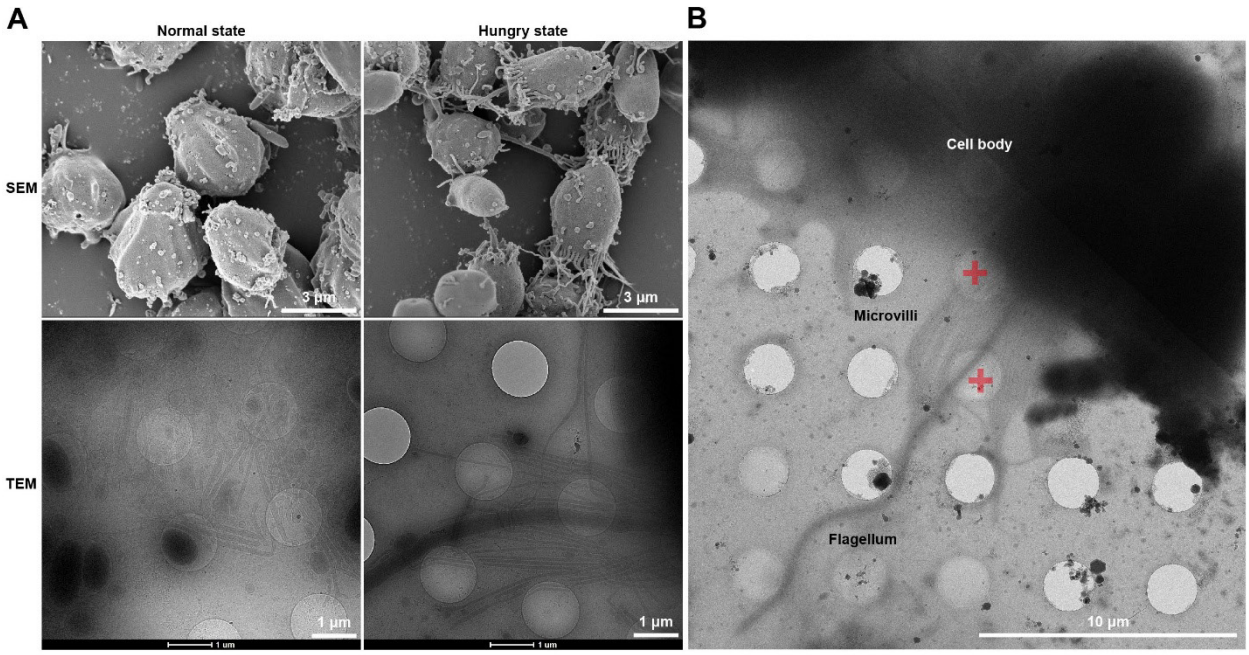


Figure S2. Optimization of cryo-EM sample for *S. rosetta* microvilli

(A) Morphological comparison of *S. rosetta* cells cultured under normal and starvation conditions. Top, room-temperature SEM illustrates that in the normal state the microvilli are largely detached, whereas under starvation they remain relatively intact. Bottom, representative cryo-EM images of vitrified samples. Under normal conditions, samples exhibited substantial bacterial contamination in the background, and the microvilli were frequently broken or fragmented. Starved samples displayed a cleaner grid background, with microvilli that were more relaxed, extended, and readily distinguishable. Scale bars, 3 µm (SEM) and 1 µm (cryo-EM). **(B)** Representative low-magnification cryo-EM image of a starved *S. rosetta* cell. The cell body, flagellum, and microvillar collar are readily distinguishable. Red crosses indicate regions suitable for high-resolution data collection from isolated microvilli. Scale bar, 10 µm.

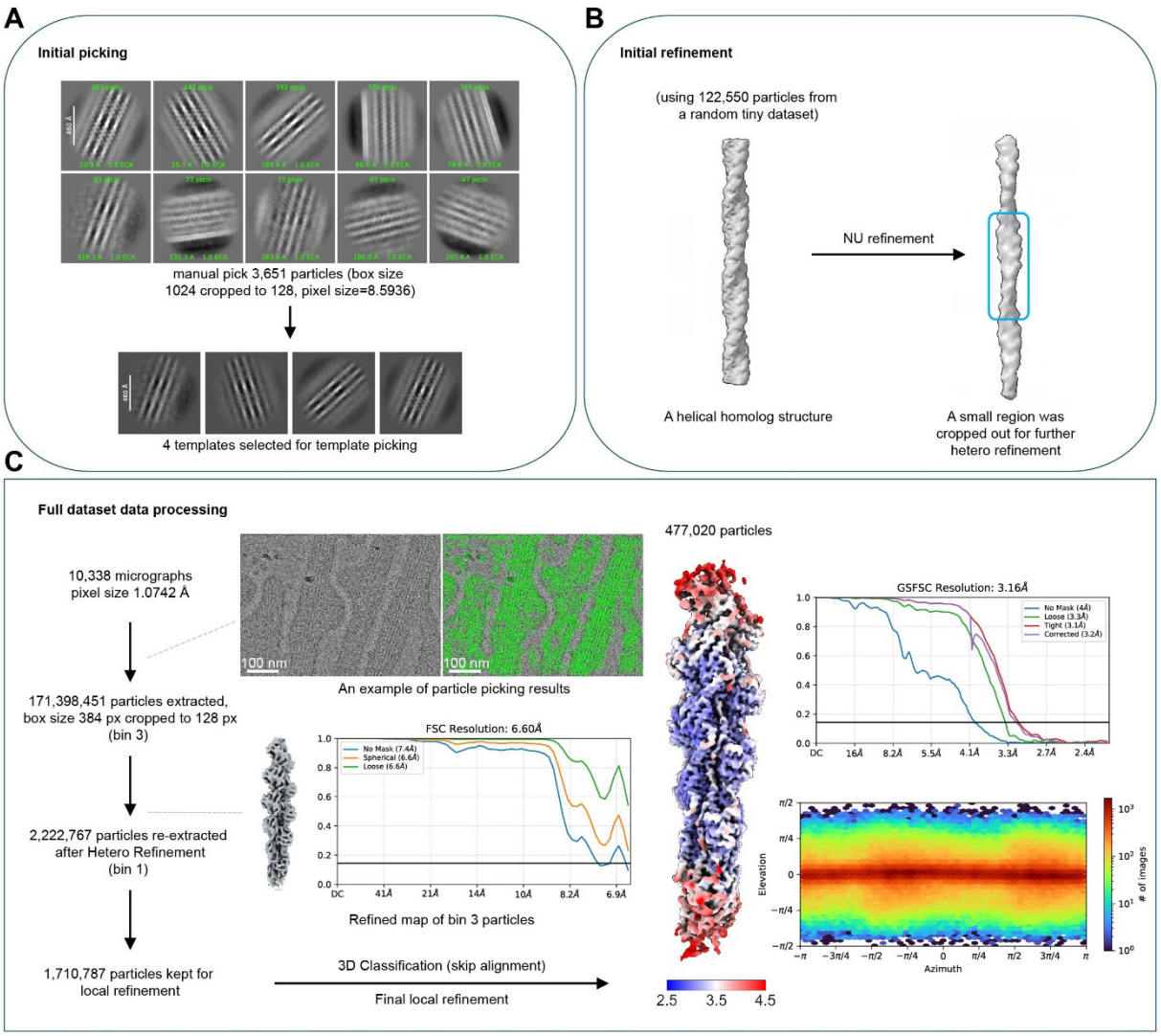


Figure S3. Cryo-EM single-particle processing workflow for *S. rosetta* microvillar F-actin

(A) Initial manual picking and template generation (top left): A total of 3,651 particles were manually picked from micrographs. Representative manually picked particles are shown. Four high-quality 2D classes were selected as templates for subsequent template-based particle picking. **(B)** Initial refinement from a small subset (top right): Using 122,550 particles randomly selected from a tiny subset of micrographs, an initial helical homolog structure was generated. **(C)** Full-dataset processing. The FSC curves (no mask, loose mask, tight mask) and the corrected curve are

shown. Local resolution estimation (2.5-4.5 Å) and the 3D directional FSC plot demonstrate anisotropy and directional resolution distribution. Please refer to the method section for detail.

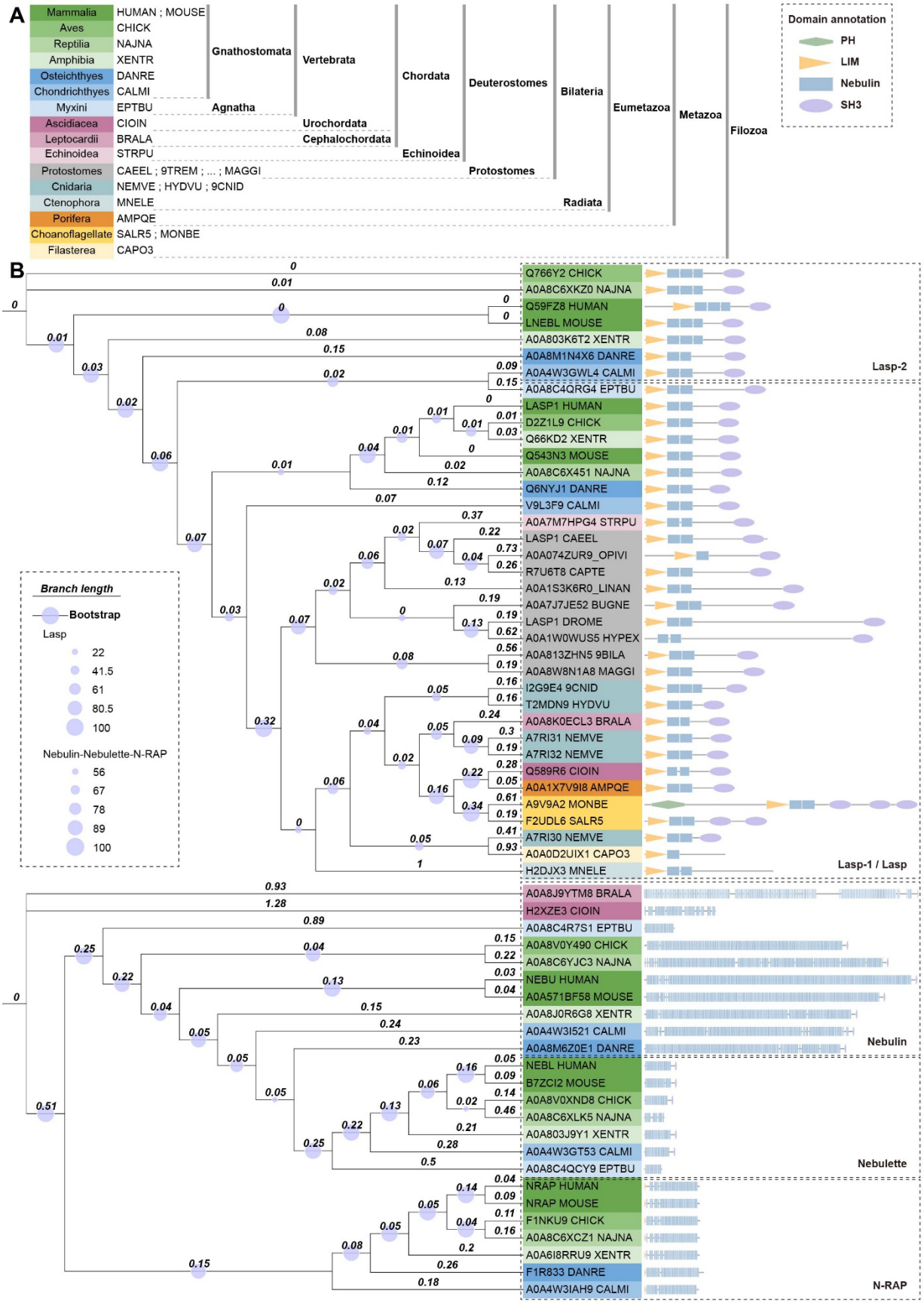

A
Mammalia
Aves
Reptilia
Amphibia
Osteichthyes
Chondrichthyes
Myxini
Ascidiacea
Leptocardii
Echinoidea
Protostomes
Cnidaria
Ctenophora
Porifera
Choanoflagellate
Filasterea
HUMAN ; MOUSE
CHICK
NAJNA
XENTR
DANRE
CALMI
EPTBU
CIOIN
BRALA
STRPU
CAEEL ; 9TREM ; ... ; MAGGI
NEMVE ; HYDVU ; 9CNID
MNELE
AMPQE
SALR5 ; MONBE
CAPO3
Gnathostomata
Agnatha
Vertebrata
Urochordata
Cephalochordata
Chordata
Echinoidea
Deuterostomes
Protostomes
Bilateria
Radiata
Eumetazoa
Metazoa
Filozoa
Domain annotation
PH
LIM
Nebulin
SH3
B
Q766Y2 CHICK
A0A8C6XKZ0 NAJNA
Q59FZ8 HUMAN
LNEBL MOUSE
A0A803K6T2 XENTR
A0A8M1N4X6 DANRE
A0A4W3GWL4 CALMI
Lasp-2
A0A8C4QRG4 EPTBU
LASP1 HUMAN
D2Z1L9 CHICK
Q66KD2 XENTR
Q543N3 MOUSE
A0A8C6X451 NAJNA
Q6NYJ1 DANRE
V9L3F9 CALMI
A0A7M7HPG4 STRPU
LASP1 CAEEL
A0A074ZUR9_OPIVI
R7U6T8 CAPTE
A0A1S3K6R0_LINAN
A0A7J7JE52 BUGNE
LASP1 DROME
A0A1W0WUS5 HYPEX
A0A813ZHN5 9BILA
A0A8W8N1A8 MAGGI
I2G9E4 9CNID
T2MDN9 HYDVU
A0A8K0ECL3 BRALA
A7RI31 NEMVE
A7RI32 NEMVE
Q589R6 CIOIN
A0A1X7V9I8 AMPQE
A9V9A2 MONBE
F2UDL6 SALR5
A7RI30 NEMVE
A0A0D2UIX1 CAPO3
H2DJX3 MNELE
Lasp-1 / Lasp
Branch length
Bootstrap
Lasp
22
41.5
61
80.5
100
Nebulin-Nebulette-N-RAP
56
67
78
89
100
A0A8J9YTM8 BRALA
H2XZE3 CIOIN
A0A8C4R7S1 EPTBU
A0A8V0Y490 CHICK
A0A8C6YJC3 NAJNA
NEBU HUMAN
A0A571BF58 MOUSE
A0A8J0R6G8 XENTR
A0A4W3I521 CALMI
A0A8M6Z0E1 DANRE
Nebulin
NEBL HUMAN
B7ZCI2 MOUSE
A0A8V0XND8 CHICK
A0A8C6XLK5 NAJNA
A0A803J9Y1 XENTR
A0A4W3GT53 CALMI
A0A8C4QCY9 EPTBU
Nebulette
NRAP HUMAN
NRAP MOUSE
F1NKU9 CHICK
A0A8C6XCZ1 NAJNA
A0A6I8RRU9 XENTR
F1R833 DANRE
A0A4W3IAH9 CALMI
N-RAP

Figure S4. Evolutionary and conservation analysis of the Nebulin family

(A) Overview of the taxonomic positions of the species used for Nebulin-family phylogenetic analysis. **(B)** Phylogenetic tree and domain annotation of Lasp, Nebulin, Nebulette, and N-RAP. Bootstrap support values are indicated by circle size, with branch lengths (substitutions per site) shown along each node. Domain architectures of each homolog mapped to the phylogeny. Proteins are annotated for LIM, PH, Nebulin repeats, and SH3 domains.

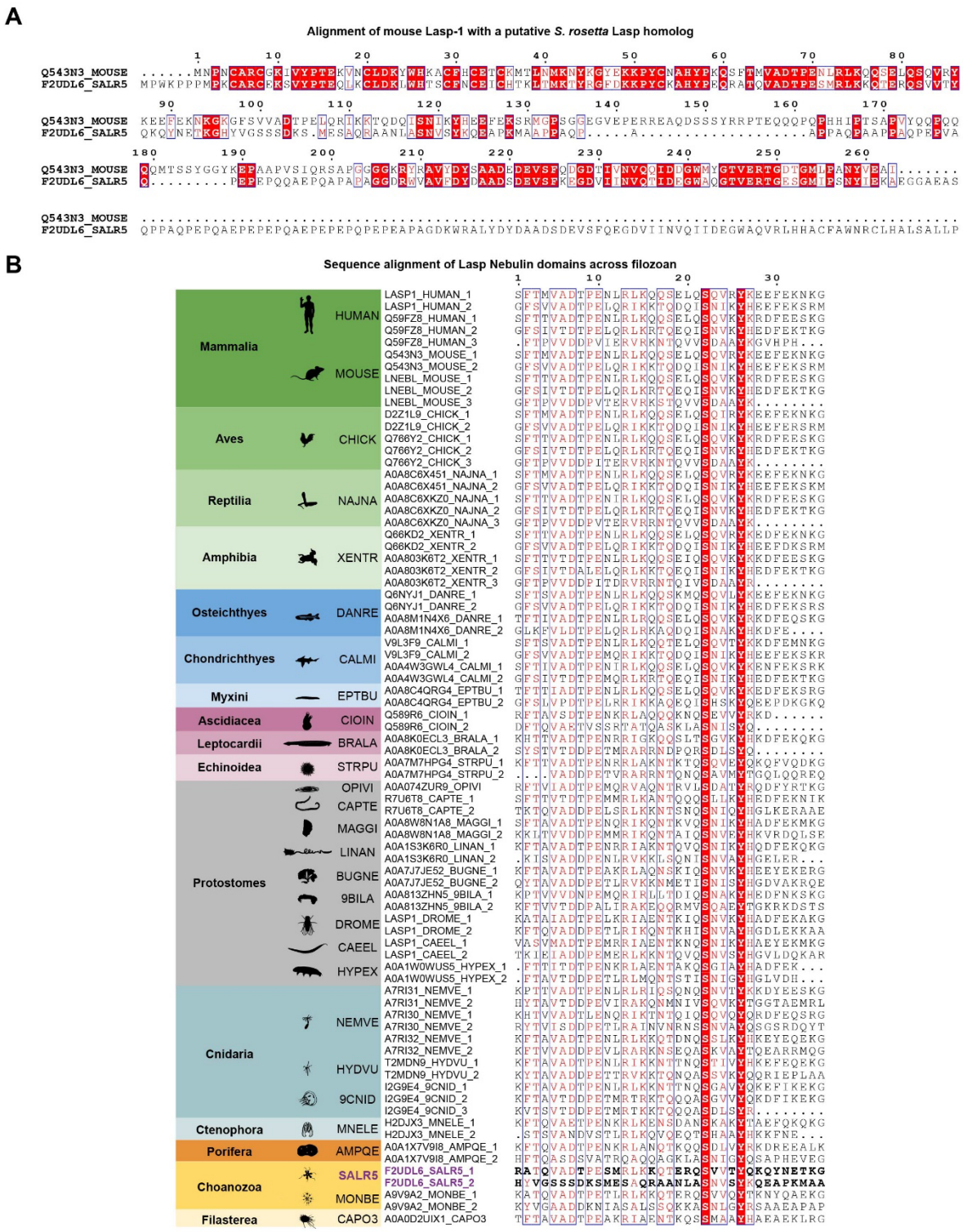


Figure S5. Identification and evolutionary conservation of a Nebulin-family protein in *S. rosetta*

(A) BLAST-based identification of a putative *S. rosetta* LASP homolog. Sequence alignment between mouse Lasp-1 (Q543N3) and *Sr*LASP (F2UDL6) reveals conservation of characteristic Lasp domains, including the LIM domain, Nebulin repeats, and SH3 domains. **(B)** Multiple sequence alignment of Lasp Nebulin domains across filozoan. Representative sequences from vertebrates, invertebrates, cnidarians, choanoflagellates, and filastereans were aligned using the Nebulin repeat region. Conserved residues characteristic of the Nebulin-family actin-binding module, including the DTPE-containing motif and the SxxxY motif, are retained across diverse filozoan lineages. Organism silhouettes were obtained from PhyloPic (https://www.phylopic.org/).

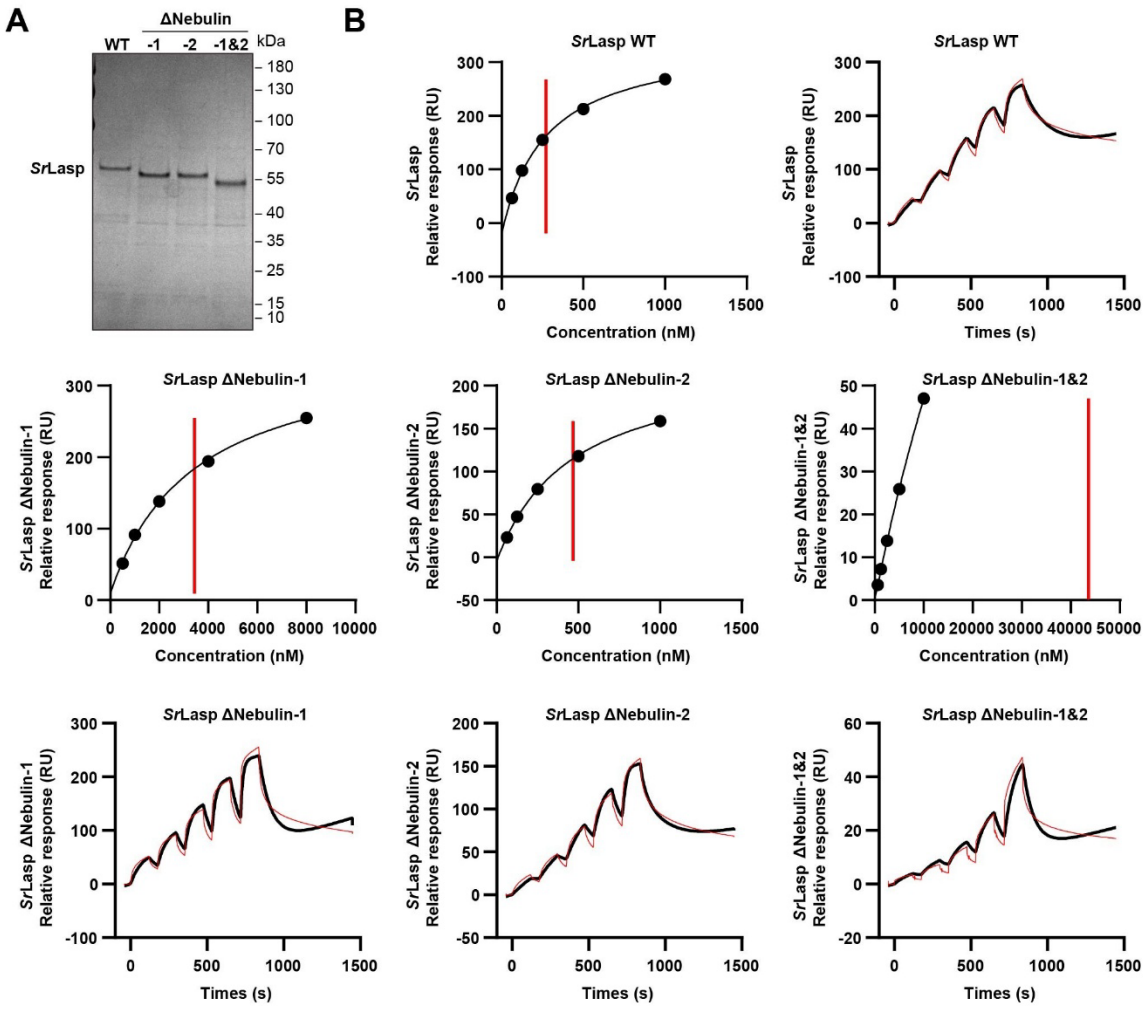


Figure S6. Characterization of *Sr*Lasp Nebulin-repeat deletion variants by SPR

(A) SDS–PAGE analysis of purified wild-type *Sr*Lasp and Nebulin-repeat deletion variants used for SPR measurements. Purified proteins were analyzed by Coomassie staining. **(B)** Affinity fitting curves from steady-state SPR analysis and representative sensorgrams from single-cycle injections are shown. Steady-state responses at the end of each injection (black dots) are plotted against analyte concentration. The black line represents the fit to a 1:1 steady-state binding model. The red vertical line indicates the fitted K_d value. The y-axis shows response units (RU), and the x-axis shows analyte concentration (nM). In representative sensorgrams, red traces indicate baseline-

corrected raw responses, and black traces show the global kinetic fit using a 1:1 Langmuir model, simultaneously fitting both association and dissociation phases across all concentrations. Each step corresponds to a sequentially increasing concentration. The y-axis represents response units (RU), and the x-axis represents time (s).

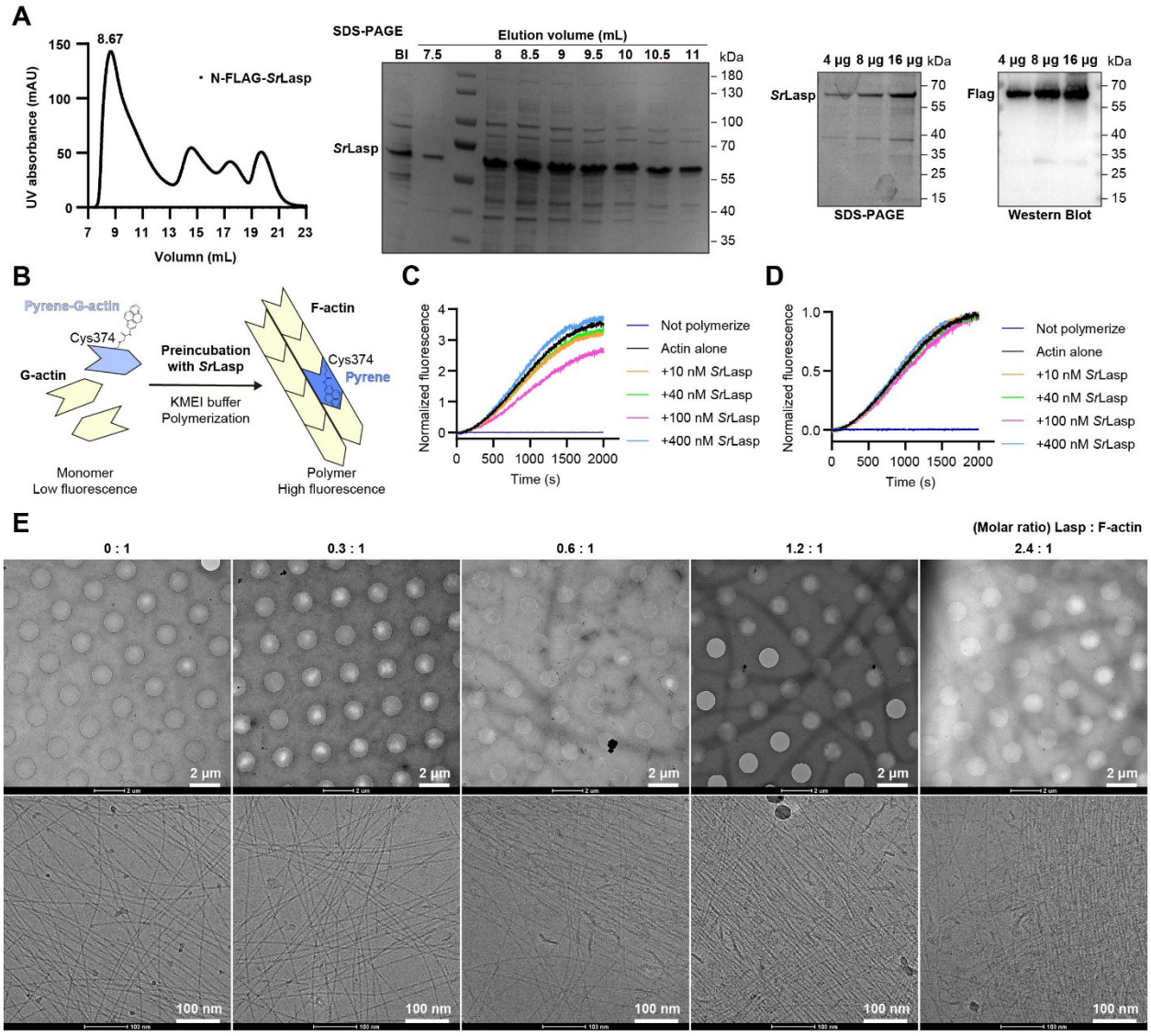


Figure S7. *Sr*Lasp can promote F-actin bundling

(A) Purification of recombinant *Sr*Lasp. Left, size-exclusion chromatography (SEC) profile showing a major *Sr*Lasp peak eluting at 8.7 mL. Middle, SDS–PAGE analysis of SEC fractions (7.5–11 mL) demonstrating protein purity. Right, SDS–PAGE and anti-FLAG immunoblot of purified *Sr*Lasp loaded at increasing amounts (4, 8, and 16 µg), confirming protein integrity and identity. **(B)** Schematic of the pyrene-actin polymerization assay. Pyrene-labeled G-actin was

preincubated with *Sr*Lasp, and polymerization was initiated by the addition of KMEI buffer. Actin polymerization was monitored by the increase in pyrene fluorescence. **(C)** Normalized pyrene-actin polymerization traces in the absence or presence of the indicated concentrations of *Sr*Lasp. Initial fluorescence intensities were aligned to that of the actin-alone control. **(D)** Independently min–max-normalized polymerization traces corresponding to (C). **(E)** Cryo-EM analysis of F-actin incubated with increasing concentrations of *Sr*Lasp. F-actin and *Sr*Lasp were mixed at the indicated *Sr*Lasp:F-actin molar ratios (0:1–2.4:1) and vitrified for imaging. Representative cryo-EM micrographs show the progressive formation of actin bundles with increasing *Sr*Lasp concentration. Top row, low-magnification views (2,700×; scale bars, 2 μm). Bottom row, high-magnification views (76,000×; scale bars, 100 nm).

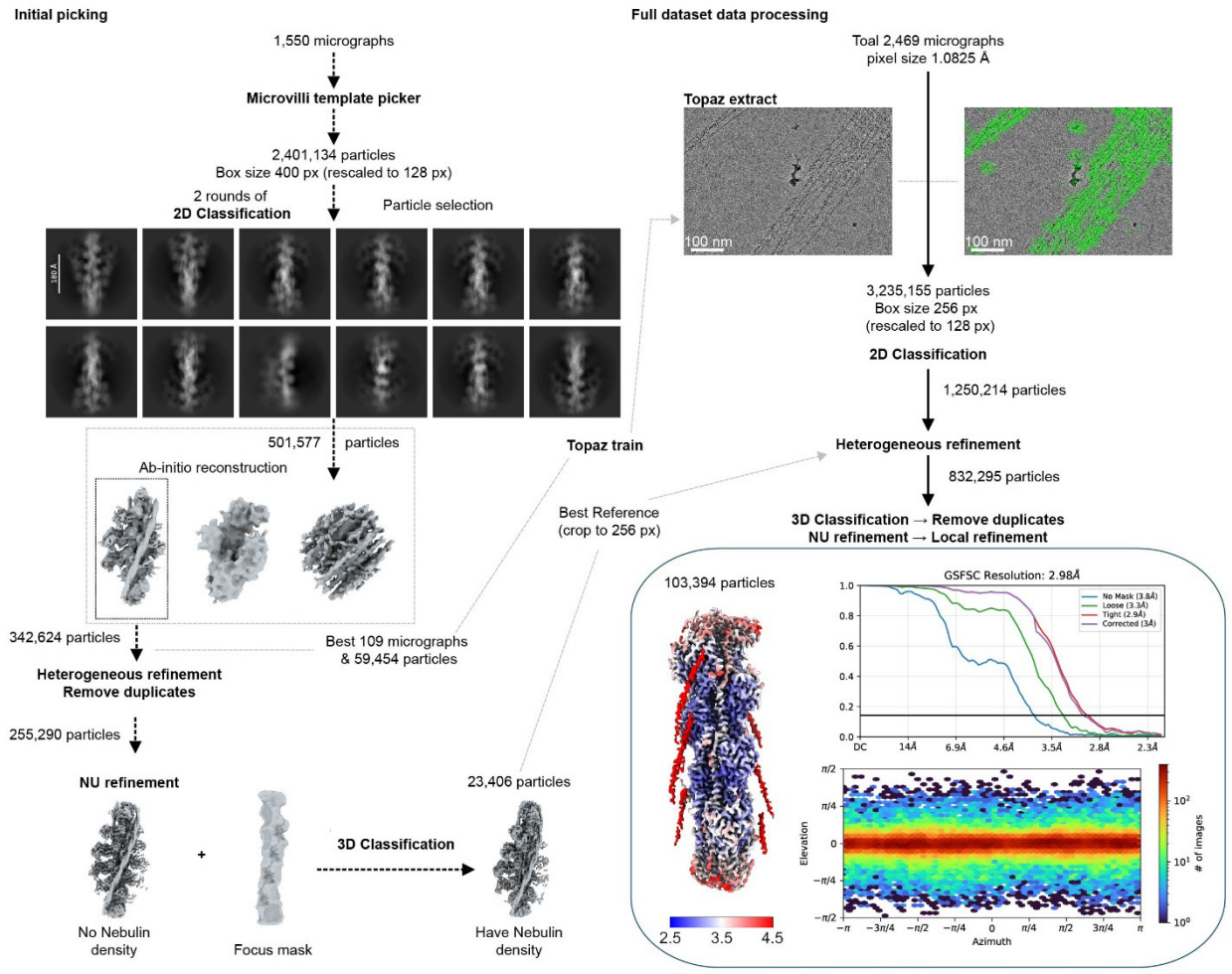


Figure S8. Cryo-EM single-particle processing workflow for mouse skeletal muscle thin filaments

Cryo-EM micrographs were subjected to template-based picking, 2D classification, and ab-initio reconstruction to obtain an initial reference for heterogeneous refinement. The full dataset was re-processed using Topaz extraction, followed by 2D/3D classification and removal of duplicates. NU-refinement and local refinement yielded the final F-actin reconstruction containing Nebulin density. The workflow, particle numbers at each step, and representative volumes are shown,

together with the GS-FSC resolution curve (2.98 Å) and directional FSC/angle-distribution analyses demonstrating isotropic map quality.

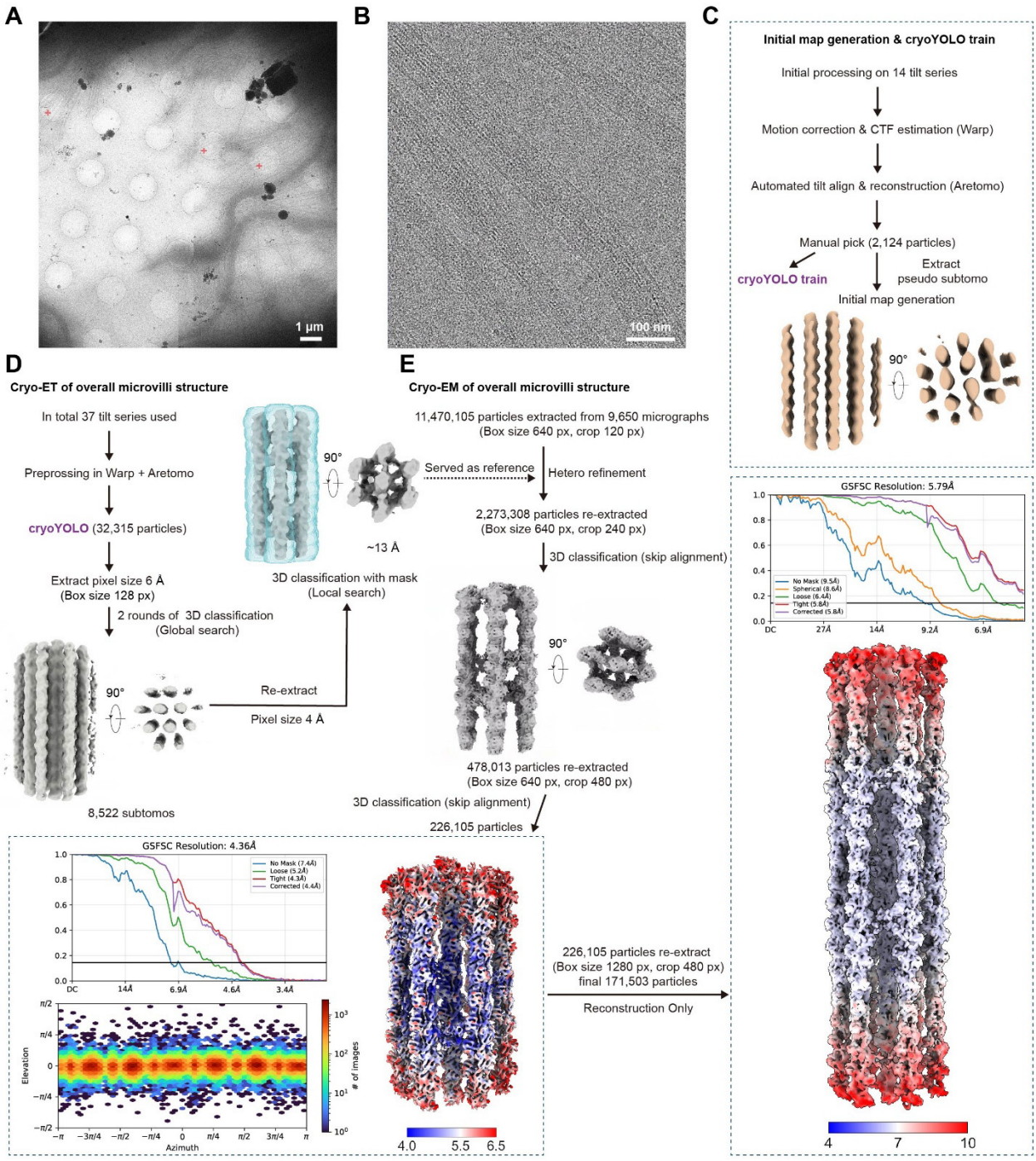


Figure S9. Cryo-ET and Cryo-EM reconstruction of *S. rosetta* microvillar F-actin bundles

(A) Representative low-magnification cryo-EM image of isolated *S. rosetta* microvilli. Red crosses indicate regions selected for tilt-series acquisition. Scale bar, 1 µm. **(B)** Representative

tomographic slice showing the ordered organization of actin filaments within a microvillar bundle. Scale bar, 100 nm. **(C)** Initial processing workflow used to generate a reference map for subtomogram averaging. Fourteen tilt series were processed by motion correction and CTF estimation in Warp, followed by tilt-series alignment and tomographic reconstruction in AreTomo. A total of 2,124 bundle segments were manually picked and used to generate an initial reference map. The resulting particle set was subsequently used to train cryoYOLO for automated particle picking. **(D)** Subtomogram averaging workflow of the overall microvilli structure. **(E)** Cryo-EM processing of the overall microvilli structure. Please refer to the method section for detail.

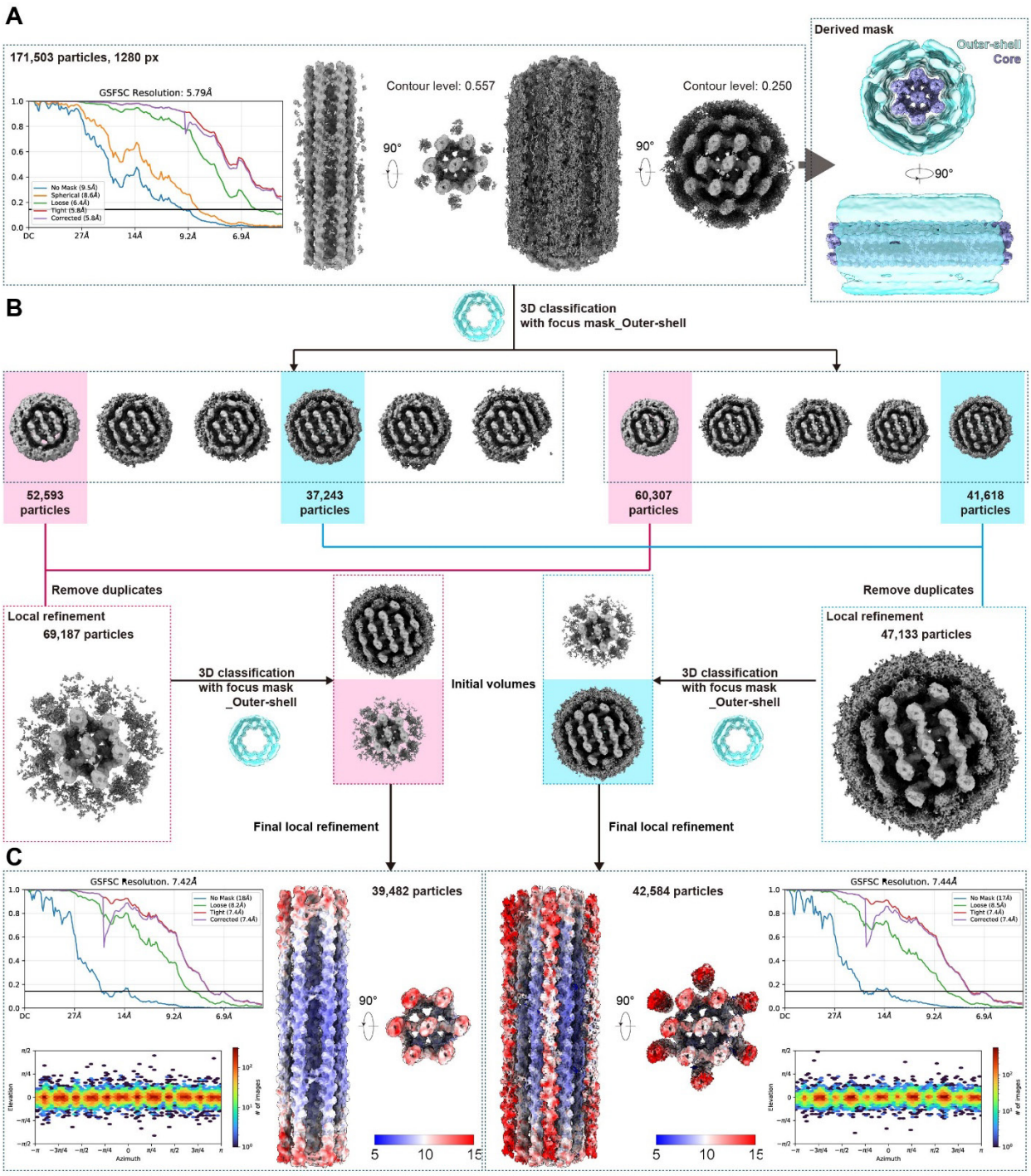


Figure S10. 3D classification and refinement of distinct microvillar actin bundle architectures

(A) Reconstruction of the microvillar actin bundle at 5.79 Å resolution from 171,503 particles extracted with a box size of 1,240 pixels, revealing additional peripheral F-actin densities at a lower contour level. Two focus masks encompassing the central core and outer shell, respectively, were generated from this reconstruction. **(B)** Workflow of 3D classification and local refinement using the outer-shell mask to distinguish seven-filament and 19-filament bundle architectures. **(C)** Final reconstructions of the seven-filament and 19-filament bundles at 7.42 Å and 7.44 Å resolution, respectively, with corresponding gold-standard FSC curves, angular distribution plots, and local resolution maps. Please refer to the method section for detail.

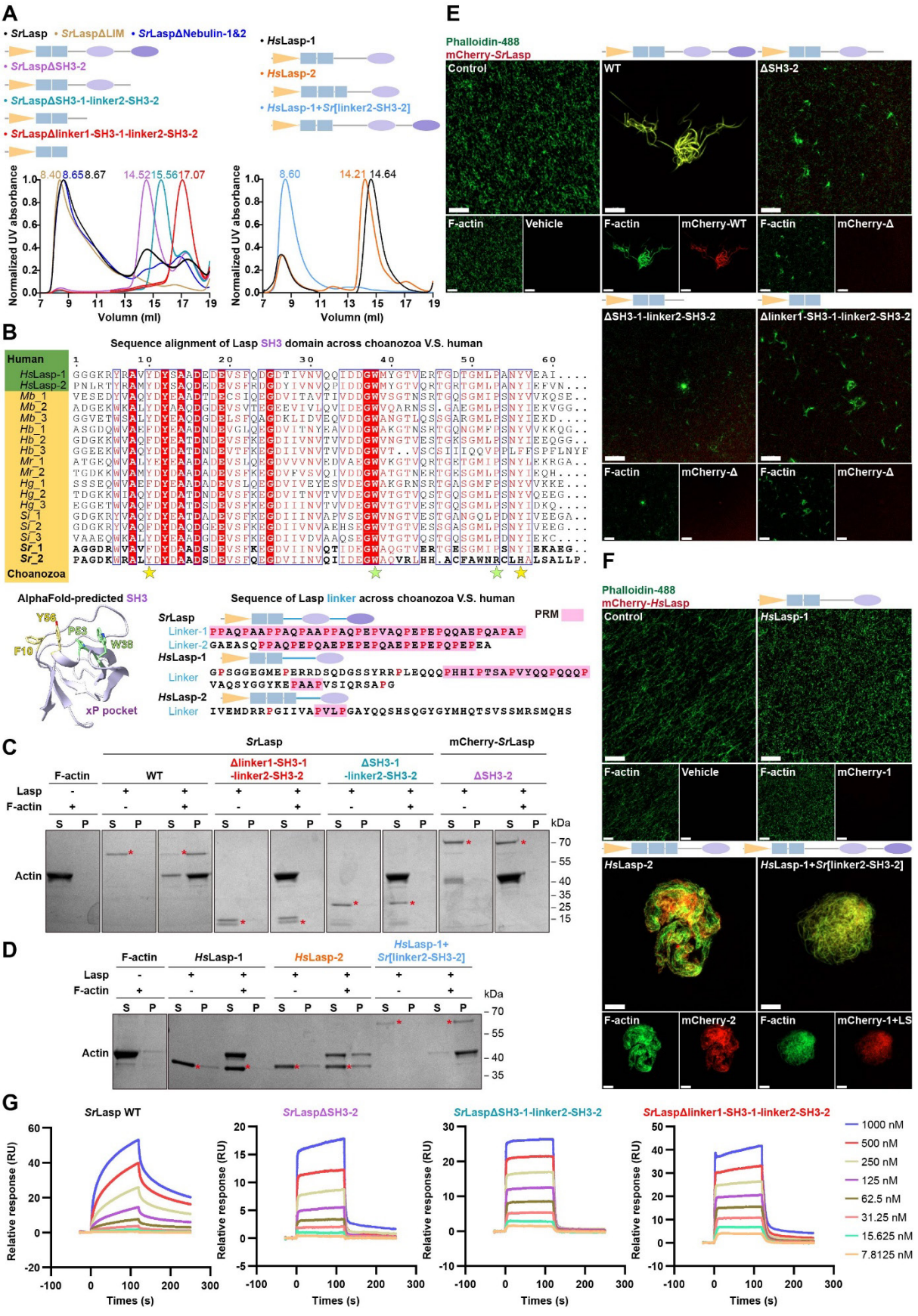

A
• SrLasp • SrLaspΔLIM • SrLaspΔNebulin-1&2
• SrLaspΔSH3-2
• SrLaspΔSH3-1-linker2-SH3-2
• SrLaspΔlinker1-SH3-1-linker2-SH3-2
• HsLasp-1
• HsLasp-2
• HsLasp-1+Sr[linker2-SH3-2]
Normalized UV absorbance
Volumn (ml)
8.40 8.65 8.67 14.52 15.56 17.07
8.60 14.21 14.64
B
Sequence alignment of Lasp SH3 domain across choanozoa V.S. human
Human
HsLasp-1
HsLasp-2
Mb_1
Mb_2
Mb_3
Hb_1
Hb_2
Hb_3
Mr_1
Mr_2
Hg_1
Hg_2
Hg_3
Sl_1
Sl_2
Sl_3
Sr_1
Sr_2
Choanozoa
AlphaFold-predicted SH3
Y56
P53
W38
F10
xP pocket
Sequence of Lasp linker across choanozoa V.S. human
SrLasp
Linker-1 PPAQPAAPPAQPAAPPAQPEPVAQPEPEPQQAEPQAPAP
Linker-2 GAEASQPPAQPEPQAEPEPEPQAEPEPEPQPEPEA
PRM
HsLasp-1
Linker GPSGGEGMEPERRDSQDGSSYRRPLEQQQPHHIPTSAPVYQQPQQQP
VAQSYGGYKEPAAPVSIQRSAPG
HsLasp-2
Linker IVEMDRRPGIIVAPVLPGAYQQSHSQGYGYMHQTSVSSMRSMQHS
C
SrLasp
mCherry-SrLasp
F-actin
WT
ΔSH3-2
Lasp
F-actin
S P
kDa
70
55
40
35
25
15
Actin
D
F-actin
HsLasp-1
HsLasp-2
HsLasp-1+ Sr[linker2-SH3-2]
Lasp
F-actin
kDa
70
55
40
35
Actin
E
Phalloidin-488
mCherry-SrLasp
Control
WT
ΔSH3-2
F-actin
Vehicle
mCherry-WT
mCherry-Δ
ΔSH3-1-linker2-SH3-2
Δlinker1-SH3-1-linker2-SH3-2
F
Phalloidin-488
mCherry-HsLasp
Control
HsLasp-1
Vehicle
mCherry-1
HsLasp-2
HsLasp-1+Sr[linker2-SH3-2]
mCherry-2
mCherry-1+LS
G
SrLasp WT
SrLaspΔSH3-2
SrLaspΔSH3-1-linker2-SH3-2
SrLaspΔlinker1-SH3-1-linker2-SH3-2
Relative response (RU)
Times (s)
1000 nM
500 nM
250 nM
125 nM
62.5 nM
31.25 nM
15.625 nM
7.8125 nM

Figure S11. SH3 domains are required for *Sr*Lasp-mediated actin bundling

(A) Size-exclusion chromatography (SEC) analysis of *Sr*Lasp, domain-deletion variants, human Lasp proteins, and chimeric constructs. Domain architectures are shown above the corresponding elution profiles. **(B)** Sequence and structural analysis of the *Sr*Lasp SH3 region. Top, multiple sequence alignment of Lasp SH3 domains from choanozoans and representative vertebrate human Lasp-1 and Lasp-2. Blast Database: Transciptome Shotgun Assembly (TSA) limited by Chonoflagellata (taxid: 28009)[27]. Conserved residues predicted to form the canonical xP-binding pocket are indicated. Bottom left, AlphaFold-predicted structure of the *Sr*Lasp SH3 domain highlighting residues that contribute to the putative xP-binding pocket. Bottom right, comparison of linker sequences from *Sr*Lasp, human Lasp-1 and Lasp-2. Putative proline-rich motifs (PRMs) are highlighted. Choanozoa: *Mb*, *Monosiga brevicollis*; *Hb*, *Hartaetosiga balthica*; *Mr*, *Microstomoeca roanoka*; *Hg*, *Hartaetosiga gracilis*; *Si*, *Salpingoeca infusionum*; and *Sr*, *Salpingoeca rosetta*. (**C**, **D**), Low-speed co-sedimentation analysis of *Sr*Lasp variants, human Lasp proteins, and chimeric constructs. Proteins were incubated with F-actin and subjected to low-speed centrifugation. Supernatant (S) and pellet (P) fractions were analyzed by SDS–PAGE. Deletion of the SH3-containing region abolished bundling activity, whereas human Lasp-2 and a chimeric Lasp-1 construct containing the *Sr*Lasp linker2–SH3-2 region promoted actin bundle formation. (**E**, **F**), Fluorescence microscopy analysis of actin bundle formation induced by *Sr*Lasp variants, human Lasp proteins, and chimeric constructs. Alexa Fluor 488–phalloidin–labeled F-actin is shown in green and mCherry-tagged proteins in red. Consistent with the co-sedimentation results, deletion of the SH3-containing region abolished *Sr*Lasp-mediated bundling, whereas human Lasp-2 and the Lasp-1–*Sr*Lasp linker2–SH3-2 chimera promoted the formation of bundled actin structures. Representative images are shown. Similar results were obtained in three independent

experiments. Scale bars, 10 μm. Representative images from three independent experiments are shown. **(G)** Representative SPR sensorgrams of wild-type *Sr*Lasp and SH3-domain deletion variants binding to immobilized F-actin. Deletion of SH3 domains altered the binding kinetics, resulting in faster association and dissociation behavior compared with wild-type *Sr*Lasp.

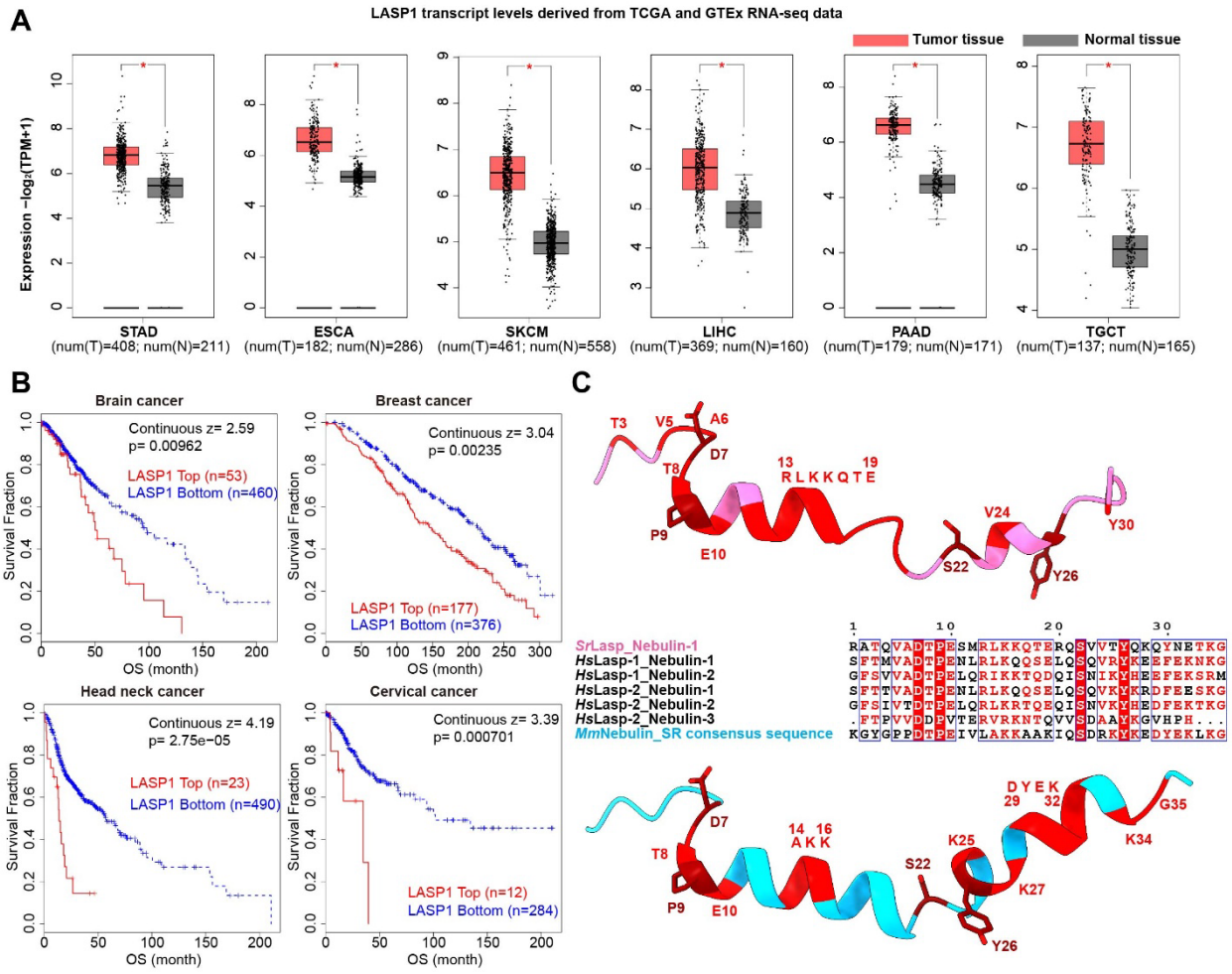


Figure S12. Conservation of Lasp Nebulin repeats and clinical relevance of human Lasp-1

(A) LASP1 transcript levels in tumor and corresponding normal tissues derived from TCGA and GTEx RNA-seq datasets. Expression levels are shown as $\log_2(TPM + 1)$. LASP1 expression is significantly elevated in multiple cancer types, including stomach adenocarcinoma (STAD), esophageal carcinoma (ESCA), skin cutaneous melanoma (SKCM), liver hepatocellular carcinoma (LIHC), pancreatic adenocarcinoma (PAAD), and testicular germ cell tumors (TGCT). Statistical significance was assessed using the indicated database analysis pipeline. *P < 0.05. http://gepia2.cancer-pku.cn/#index **(B)** Kaplan–Meier survival analysis of patients stratified by LASP1 expression level. Patients with high LASP1 expression exhibited significantly reduced

overall survival in brain cancer, breast cancer, head and neck cancer, and cervical cancer. Continuous z scores and corresponding P values are indicated in each panel. http://tide.dfci.harvard.edu **(C)** Structural and sequence comparison of Nebulin-family Nebulin repeats. Top, atomic model of the actin-bound *Sr*Lasp Nebulin-1 repeat with key interface residues highlighted. Bottom, structural comparison between *Sr*Lasp Nebulin-1 and mouse Nebulin simple repeats (SR) consensus repeat. Conserved residues identified by sequence alignment are mapped onto the structures (red).

Table S1: Data collection and data processing of Cryo-ET

	***S. rosetta* microvilli F-actin bundle**
Data collection	
Software	SerialEM
Microscope	FEI Titan Krios
Voltage (kV)	300
Detector	Gatan K3
Total electron dose (e^{-}/Å^2)	123
Electron dose per tilt(e^{-}/Å^2)	2
Tilt scheme	Dose-symmetric scheme
Tilt range (°)	-60~60
Tilt increment (°)	3
Defocus range (μm)	-5~-3
Magnification	53,000
Pixel size (Å)	1.6544
Data processing	
Software	Warp; Aretomo; RELION
Symmetry imposed	C1
Tilt series (no.)	37
Initial particle images (no.)	32,315
Final particle images (no.)	8,522
Map resolution (Å)	13

Table S2: Data collection, refinement and model building statistics of Cryo-EM

	S. rosetta microvilli single F-actin	*M. musculus* skeletal thin-filament	*S. rosetta* microvilli F-actin bundle	
			Short	Long
Data collection				
Software	AutoEMation			
Microscope	FEI Titan Krios			
Voltage (kV)	300			
Detector	Gatan K3			
Electron exposure (e^{-}/Å^2)	50			
Defocus range (μm)	-2.0~-1.5			
Magnification	81,000			
Pixel size (Å)	1.0742	1.0825	1.0742	
Data processing				
Software	CryoSPARC			
Symmetry imposed	C1			
Micrographs (no.)	10,338	2,469	9,650	
Final particle images (no.)	477,020	103,394	226,105	171,503
Map resolution (Å)	3.16	2.98	4.36	5.79
Refinement				
Software	COOT & PHENIX			
Model composition				
Non-hydrogen atoms	25,598	19,040		
Protein residues	3,238	2,436		
Ligands	ATP、Mg^{2+}			
B factors (Å^2)				
Protein	160.88	134.25		
Ligand	148.60	130.77		
R.m.s. deviations				
Bond lengths (Å)	0.003	0.003		
Bond angles (°)	0.762	0.680		
Validation				
MolProbity score	1.72	1.49		
Clashscore	8.28	7.53		
Rotamer outliers (%)	0.84	0.80		
Ramachandran plot				
Favored (%)	96.10	97.63		
Allowed (%)	3.71	2.12		
Outliers (%)	0.19	0.25		

Movie S1

S. rosetta cells cultured under standard feeding conditions

Movie S2

S. rosetta cells after starvation

Movie S3

Three-dimensional architecture of the *S. rosetta* microvilli

Movie S4

Periodic organization and structural plasticity of *Sr*Fascin crosslinks